Space Weather

RESEARCH ARTICLE
10.1029/2019SW002342

Special Section:
Outcomes of the Applied Space Environments Conference, May 12-17, 2019, Los Angeles, CA

Key Points:
- X-ray spectra generated by energetic electrons can be used to remotely determine the electrostatic potential on a surface
- This method is experimentally demonstrated and found to accurately resolve surface potentials and elemental compositions

Correspondence to:
K. T. Wilson,
kieran.wilson@colorado.edu

Citation:
Wilson, K. T., Bengtson, M. T., & Schaub, H. (2020). X-ray spectroscopic determination of electrostatic potential and material composition for spacecraft: Experimental results. *Space Weather*, *18*, e2019SW002342. https://doi.org/10.1029/2019SW002342

Received 28 AUG 2019
Accepted 12 FEB 2020
Accepted article online 23 FEB 2020

X-ray Spectroscopic Determination of Electrostatic Potential and Material Composition for Spacecraft: Experimental Results

K. T. Wilson[1], **M. T. Bengtson**[1], **and H. Schaub**[1]

[1]Department of Aerospace Engineering Sciences, University of Colorado, Boulder, CO, USA

Abstract Remote surface potential determination for nearby objects in space is an enabling technology for a range of space mission concepts, from improved rendezvous capabilities to touchless debris remediation with the electrostatic tractor concept. One concept is to use a nearby servicing spacecraft which fires electrons at the target. These electrons generate bremsstrahlung X-rays, and the resultant X-ray spectrum can be used to determine the landing energy of the electrons. By knowing the initial energy of the electrons, such as those emitted from an electron gun, the relative potential of the target can be inferred. The use of electron-induced X-rays to determine the electrostatic potential of a surface has previously been investigated theoretically, but this work demonstrates it experimentally. Accuracy is found to correlate to the angle between the detector and the target, and investigation of this relationship is a topic of future work. The mean error in landing energy is found to be approximately 1%, and the mean error in estimated plate voltage is found to be within the uncertainty of the high voltage power supply. Material determination is successfully demonstrated, using characteristic X-rays to identify elements that make up less than 0.5% by mass of the target sample. Several possible means of improving landing energy accuracy are discussed.

1. Introduction

The space environment results in spacecraft and debris objects developing electrostatic charges and resultant potentials. This is a result of the currents in the environment, from solar radiation-induced photoelectric emission to ion and electron currents in the ambient plasma and resultant secondary electron emission from the spacecraft.

In low earth orbit these potentials are generally limited to small magnitudes due to the presence of relatively cold, dense plasma, which generally limits spacecraft charging to tens of volts negative (Lai, 2011). Auroral region crossings encountered in polar orbits can lead to potentials exceeding −2 kV due to the high fluxes of high energy particles (Anderson, 2012). However, at higher orbital regions including the valuable geostationary orbit, ambient plasma tends to be much hotter and sparser, which leads to more significant charging conditions. The SCATHA mission observed potentials of up to −30 kV and found that potentials of tens of kilovolts could be reached regularly (Mullen et al., 1986).

Elevated spacecraft potentials pose a range of problems for missions. Despite the relatively low potentials that develop in the low earth orbit, prior work has identified significant risks to astronauts on spacewalks, which prompts the use of plasma contactors throughout any extravehicular activity (Anderson, 2012; Carruth et al., 2001). GPS satellites have been shown to experience frequent charging events, resulting in arcing between solar panel components. These arcs disrupt power generation by either depositing soot on the solar panel cover glass or forming lichtenburg figures, decreasing light reaching the panels and ultimately increasing the rate of power decay far above pre-mission expectations (Ferguson et al., 2017). Arcing is a primary cause of damage to solar arrays, while damaged arrays account for half of insurance claims for spacecraft (Brandhorst & Rodiek, 2007; Katz et al., 1998).

While most effects of spacecraft charging so far observed have been limited to individual spacecraft, having multiple spacecraft flying in close proximity (such as for proposed servicing missions, like Reed et al. (2016) or the rendezvous maneuvers required for NASA's planned lunar missions) introduces new effects. Charging can complicate rendezvous and docking scenarios, as electrostatic forces and torques add perturbing dynamics to the two spacecraft. For spacecraft charged to different potentials there is also the risk of arcing as they rendezvous, which can damage electronics and other systems (Goodman et al., 2019).

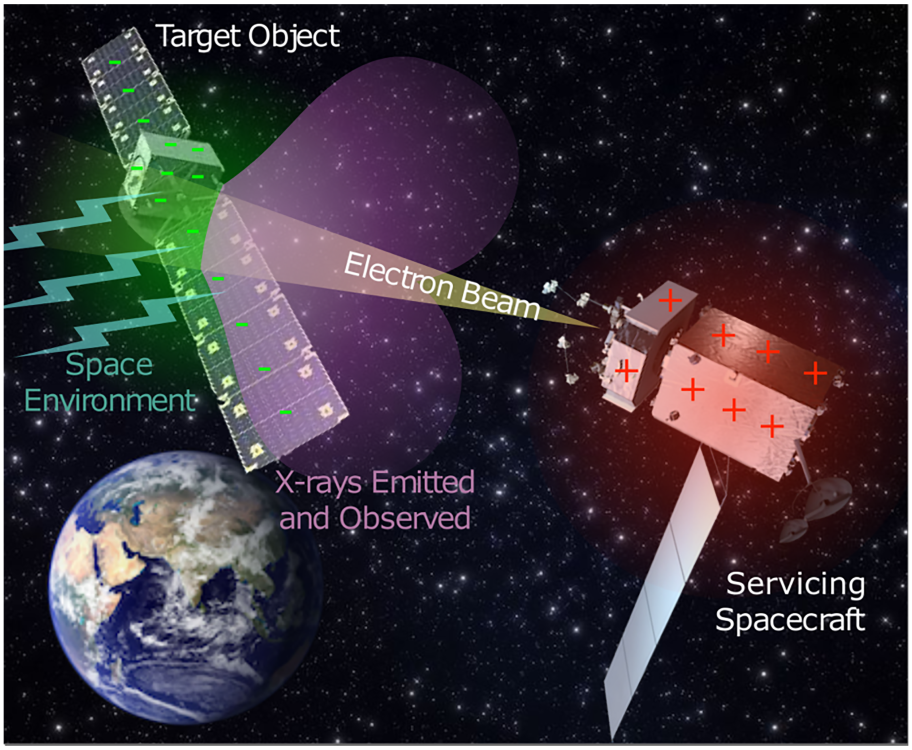

Figure 1. An illustration of the electrostatic tractor concept for reorbiting or detumbling debris objects.

Several proposals exist to harness electrostatic charging to control the relative motion between spacecraft. King et al. (2002, 2003) explore the applications of inter-spacecraft electrostatic forces for formation flying, where they can be used to maintain a formation with inter-craft spacing on the order of tens of meters without the use of propellant.

Another application of this technology is the electrostatic tractor concept presented by Schaub and Moorer (2014). The electrostatic tractor seen in Figure 1 serves as a means of reorbiting hazardous space debris, such as defunct craft at geostationary orbit, without making physical contact. Studies have shown that these defunct craft can have tumble rates of tens of degrees per second, which makes any effort to physically grapple these objects very hazardous (Karavaev et al., 2004). Instead of directly grasping an uncontrolled object, the electrostatic tractor utilizes an electron gun mounted on a servicing craft to modulate the potential of the servicer and the target object. By doing so, the servicer can generate forces of up to 10 mN from distances of over 10 m (Bengtson et al., 2018). It can then utilize the electrostatic forces and torques developed between the two craft to either detumble the target to allow for physical contact (enabling servicing) or to touchlessly move into a safe graveyard orbit over a period of weeks. Hogan (2014) shows that an accurate charge model is important, as the feedback control can become unstable if the target potential is mis-modeled.

The ability to remotely measure the potential on an object in space is an enabling technology for many of these mission architectures. Additionally, this ability could be used to monitor or mitigate risks of arcing during rendezvous and improve knowledge about spacecraft charging through in situ observations.

A few prior proposals exist for determining the charge on an object remotely. Bennett (2017) suggests determining the relative charge on a space object by comparing its orbital motion to that of a nearby object of known charge; by examining how the object's motion is perturbed over a period of minutes or hours, it is possible to determine a single point estimate of the relative potential on the unknown body. Engwerda (2017) proposed measuring electric fields in the vicinity of a spacecraft to determine the electrostatic potential and charge distribution on a nearby object. This work was focused on generating a multisphere representation of the charge on the target object from sensed electric fields; however, it neglected the challenges of electric field sensing in a sparse plasma environment.

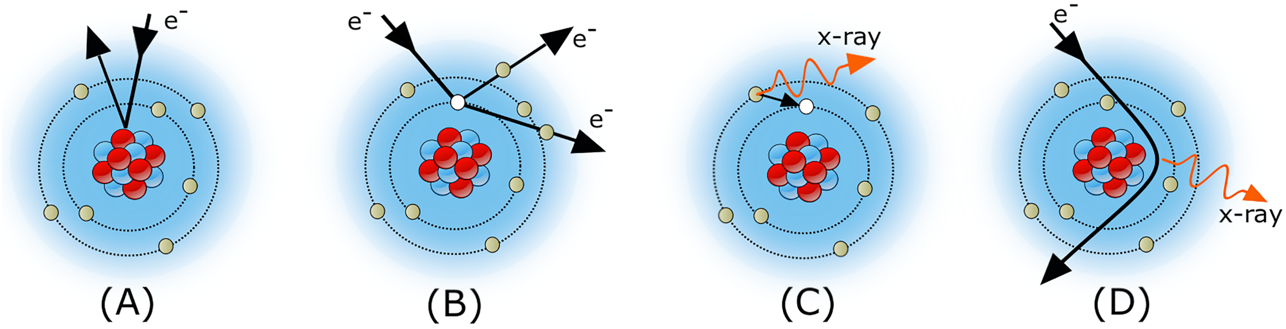

Figure 2. Interactions between impinging electrons and atoms. (a) Incident electron is backscattered. (b) Electron removes inner shell electron from atom (secondary electron emission). (c) Electron relaxes to fill inner shell vacancy and releases characteristic X-ray. (d) Electron is accelerated in vicinity of nucleus and releases a bremsstrahlung X-ray (Wilson & Schaub, 2019).

The electron microscopy field has long had challenges associated with surface charge buildup as a result of electron bombardment and have consequently developed a range of methods to determine the surface potential of a sample without physically contacting it (Belhaj et al., 2001; Cazaux, 2008; Heath et al., 2012). One method is that of examining the electron energy spectra to find a peak generated by secondary electrons, which are born on the target surface with near-zero energy. Therefore, the energy the electrons acquire prior to capture is equivalent to the potential difference between the surface and the detector. This method is applied to sense lunar surface charging by Halekas et al. (2007) and is examined in spacecraft scenarios by Bengtson et al. (2019) and experimentally by Bengtson and Schaub (2019).

Another approach relies on the X-ray spectra generated by bremsstrahlung radiation as seen in Figure 2d. As electrons interact with atoms, the energy lost in each interaction is emitted as an X-ray photon through bremsstrahlung radiation. These X-rays form a continuum in energy as seen in Figure 4, with an upper limit given by the Duane-Hunt law as the landing energy of the incident electrons (Duane & Hunt, 1915). Therefore, this spectrum can be used to establish the landing energy of the electrons. If the initial energy of the electrons leaving the gun are known, then the change in energy to landing can be used to determine the potential difference between the source and the target. These X-rays have unique energies that can be used to identify the specific element they come from, which enables material identification as well as surface potential determination. Ferguson et al. (2014) propose a series of methods to remotely detect signatures of charging events. Among these methods, they suggest that it may be possible to detect a spacecraft passing through a region of high energy electron fluxes by looking for bremsstrahlung X-rays from a co-orbiting observatory, which would provide a remote indication of a likely charging event. However, this method would not provide any information on the magnitude of charging. The use of X-ray spectra to determine surface potentials is analyzed theoretically in Wilson and Schaub (2019), and experimental validation of this method is the focus of the current work. In addition to bremsstrahlung radiation, energetic electrons interacting with a surface also result in the emission of characteristic X-rays, which are a standard method to identify the elemental composition of a surface (Van Grieken & Markowicz, 2002).

2. Theoretical Overview

Energetic electrons, those with energies above a few hundred electron volts, can interact with atoms through a few dominant mechanisms. These electrons will often go through a series of interactions with different atoms before expending their kinetic energy. Backscatter, as seen in Figure 2 furthest left, results in an incident electron preserving most of its initial kinetic energy but being deflected out of the material , primarily through elastic interactions with the nucleus. When inner shell electrons are removed by interaction with an incident electron, the resultant electron configuration is energetically unstable. An outer shell electron then relaxes to fill the vacancy, and the energy difference between the shells is released as a characteristic X-ray specific to the element of origin. This process can also result in the ejection of an Auger electron, the energy of which can be used to identify the source element.

Of particular interest to this work, bremsstrahlung radiation occurs primarily when an electron passes close to an atomic nucleus and is slowed by the interaction, though it also occurs during backscatter events. The energy lost in this interaction is emitted as an X-ray. Because there are an infinite number of paths for an

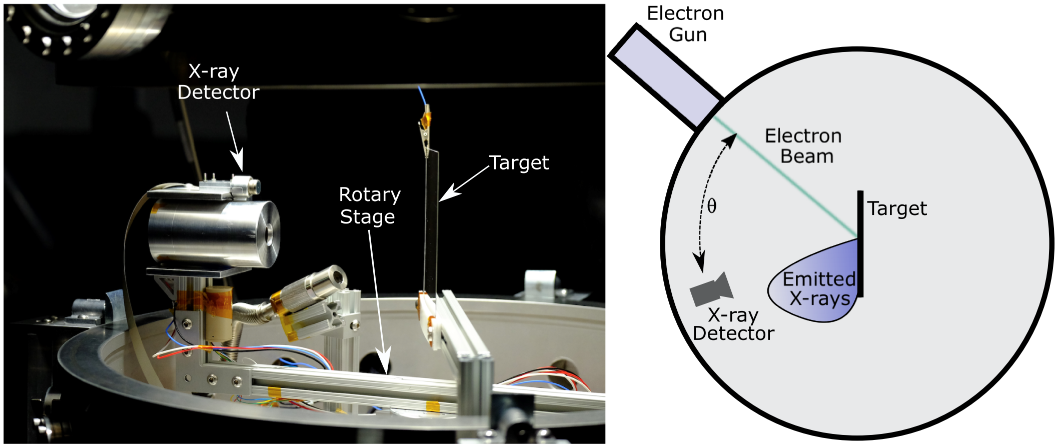

Figure 3. Left: Photograph of experimental setup in chamber. Right: Top-down schematic of components inside chamber. The chamber is 60 cm in diameter, and the X-ray detector is approximately 20 cm from the target plate.

electron to take in the vicinity of the nucleus, the energy loss and resultant X-rays form a continuum. The upper energy limit for this spectrum is given by the Duane-Hunt law, as the largest energy change is the case where an incident electron is fully stopped in a single interaction (Duane & Hunt, 1915). Therefore, the bremsstrahlung X-ray spectrum will have no photons above the landing energy of the electrons, a property that can be utilized to determine the electron's landing energy.

If the initial energy of the electrons–either emitted from the electron gun or present in the ambient plasma–are known, then the change from initial energy to landing energy can be used to establish the potential difference between the source and the target.

3. Experimental Description

The experimental setup consists of three primary components: an electron gun aimed at a target plate and an X-ray detector to observe the resultant X-ray spectra (Figure 3). The electron gun, a Kimball Physics EMG-4212D, is capable of accelerating electrons up to 30 keV. An Inconel-625 (a high temperature nickel alloy) target plate was used for all experiments. This material is commonly used in spacecraft engines and has the advantage of being an alloy composed of a range of elements with distinct characteristic peaks ranging from 2 to 16 keV (Deslattes et al., 2005). This range allows real-time verification of X-ray detector calibration at multiple energies. The potential of the plate is controlled by an independent high voltage power supply (a Spellman CZE200) with a range of ±30 kV and an accuracy of ±30 V.

An Amptek X123 X-ray spectrometer with a 6 mm^2 Si-PIN diode sensor is used to detect the generated X-rays. This unit is compact, lightweight, and low-power, which reduces the amount of heat that must be removed from the system when operating in the vacuum chamber. In addition, this detector has spaceflight heritage as the primary instrument on the Mini-XSS solar observatory mission (Moore et al., 2018). Detector calibration was accomplished in atmosphere with an Fe-55 radioisotope source. This isotope emits X-rays at two energies, 5.89 and 6.49 keV, which are used to create a linear calibration for the detector under specific operating settings. The detector also has a 0.0254 mm thick beryllium frontal window. This beryllium window prevents stray photons from entering the detector, effectively attenuating any photons below 0.9 keV. In addition to a lower limit, the detector efficiency also decreases as the energy increases above 12 keV, due to photons passing through the active volume of the Si-PIN detector without depositing all of their energy (Xr-100cr Si-PIN X-ray detector, 2018).

The noise threshold of the detector increases with increasing temperature, so an integrated thermoelectric cooler is used to maintain acceptably low noise levels. For these experiments a temperature of 240 K was maintained at the diode. While this represented somewhat higher noise and reduced resolution relative to the minimum achievable temperature of 217 K, this temperature could be maintained for several hours at a time in the vacuum environment without running into thermal saturation of the heat sink. Therefore, long duration sweeps and experiments could be conducted without detector characteristics varying during testing.

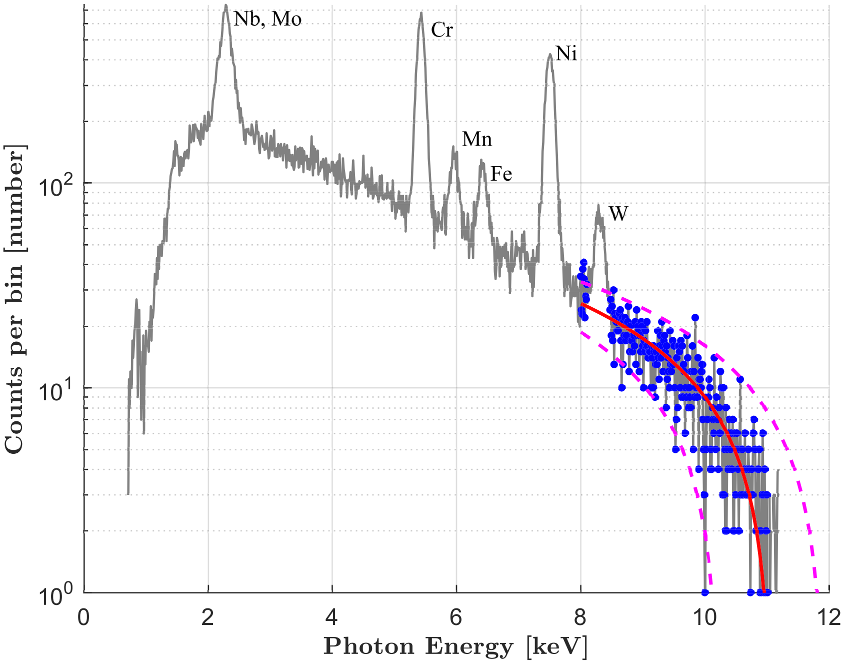

Figure 4. Spectrum from 11 keV electrons on Inconel, with line of fit (solid red), uncertainty bounds (dashed magenta), and high energy data used for the fit (blue points).

The detector is mounted on a rotational stage which allows the generated spectrum to be observed from a range of angles. Approximately 120° were open to sweep between the electron beam and the target plate, and this range was sampled at even increments (10° between samples). The detector was mounted at the same height as the electron beam. The angle closest to the electron beam was the starting position for sweeps and came at 15° of angular separation from the beam; interference with the electron beam prevented the detector from reducing this separation further. The maximum angle between the detector and the electron beam is near parallel to the target plate. The position of the detector relative to the electron beam was determined by analyzing top-down images of the experimental setup using the open source image analysis tool FIJI, which is built upon the widely used, open source ImageJ (Schindelin et al., 2012).

For each test, the electron gun was set to a desired beam energy and current (both of which were held constant for the duration of the test), while the potential of the target plate and the angle of the detector were varied. All experiments were conducted at a pressure of 1×10^{-6} Torr or lower, with a beam current of 10 μA. Power supplies, instruments, and the electron gun were allowed to warm up and equilibriate in accordance with their manuals prior to data collection.

4. Results and Discussion

Figure 4 shows the spectrum generated by an 11 keV incident beam on an inconel target. The potential of the plate was controlled by a high voltage power supply and maintained at 0 V in this test. Potentials are all measured relative to a common ground connected to the building grounding system and is used as a ground reference for the chamber walls, the power supplies, and the electron gun. The low energy part of the spectrum, which is below about 2 keV, is largely attenuated by the beryllium detector window, yielding little useful data in this region. The lower limit of detection could be reduced by utilizing a thinner beryllium window than the 0.0254 mm version used in this detector; this would allow spectral lines of elements lighter than chlorine to be detected (Deslattes et al., 2005).

There are a series of peaks visible between 2 and 9 keV, which correspond to discrete electron orbital transitions in specific elements. The lowest peak, centered at 2.21 keV, corresponds to the L_α orbital transitions in Niobium (2.169 keV) and Molybdenum (2.292 keV) (Deslattes et al., 2005). These lines cannot be independently resolved for the chosen detector settings; however, the presence of two separate spectral lines in this region is evidenced by the increased peak width. For a discrete spectral energy, such as the characteristic

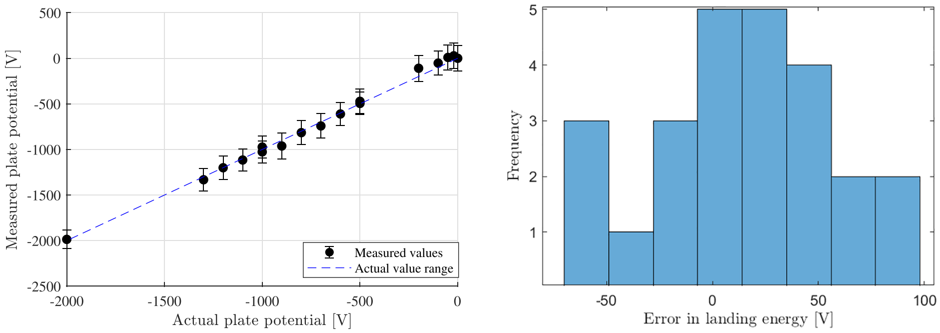

Figure 5. Left: Estimated plate potential measured at the +50° angle. Right: Error for the set of points shown in the left plot.

radiation emitted by an element, the detector will observe the impulse as a Gaussian curve with a finite width and an observed mean x_o equal to the characteristic energy. The amount that the impulse is spread out is generally described using the width of the Gaussian peak at half of its maximum value, usually referred to as the full width at half maximum (FWHM). For this peak, the FWHM is 280 eV, while the other characteristic peaks , labeled in Figure 4, all have a FWHM of 150–170 eV and correspond to K_α transitions (with the exception of tungsten, which is also a L_α transition). Conversion of FWHM values to the more broadly familiar standard deviation can be achieved using the relation

$$\sigma = \frac{\text{FWHM}}{2\sqrt{2\ln 2}}. \tag{1}$$

Per the Duane-Hunt law, the landing energy of the incident electrons can be determined by observing the highest energy photon emitted from the sample (Duane & Hunt, 1915). In theory, this upper threshold will correspond to the case where an incident electron is fully stopped in a single interaction with an atom, resulting in the electron's entire landing energy being emitted in a single photon. As seen in Figure 4, the number of counts decays with increasing energy, approaching the 11 keV landing energy of the electrons as expected. However, in practice, this can be difficult to ascertain; in addition to the vanishingly small number of electrons undergoing just one collision, physical detectors also observe noise as well as actual photon events. In addition, the sun contributes a significant amount of X-ray radiation to the space environment, which may contaminate the spectrum of photons generated by the electron beam and observed by the sensor. Therefore, this approach is unlikely to be robust.

Instead, an alternative approach to determining the landing energy of a monoenergetic electron beam from the resultant bremsstrahlung spectrum is described by Lamoureux and Charles (2006). A region near the upper limit, illustrated in Figure 4 by blue points, is selected and a line of best fit determined for this data range. The interception of this line with the x-axis corresponds to the estimated landing energy. The line of best fit is illustrated by the solid red curve, while the dashed lines represent curves which encompass 95% of the experimental data points. These bounding curves are used to establish a measure of uncertainty for the best fit curve. This approach is valid only for the bremsstrahlung continuum, so the contributions of characteristic peaks must be removed prior to line fitting. This was achieved by applying a lowpass filter to the data to reduce stochastic noise and then using the Matlab `findpeaks` function where width thresholds were selected based on the expected FWHM for the detector to minimize the number of false positive results. For this case, the commanded electron gun energy was 11.000 keV, with a beam current of 10 μA and a plate potential of 0 V, and the landing energy determined by this method is 11.071 keV. The confidence bounds are used as a measure of the uncertainty in the landing energy estimate, or ±0.175 keV here. The points and lines shown in Figure 4 are based on the raw, unfiltered data. Applying a lowpass filter reduces the noise, and results in lower computed uncertainty bounds.

For energies $>$ 12 keV the detector efficiency begins to decrease as photons can fully penetrate the Si-PIN detector without depositing all of their energy. As a result, a first-order line may no longer be the best fit solution to determining landing energy above this range; experiments conducted here were kept below 12 keV to avoid these detector-specific issues. The power supplies used were considered unreliable at potentials above 2,000 V but had an uncertainty of ±30 V up to 2,000 V. Therefore, this work examines plate potentials

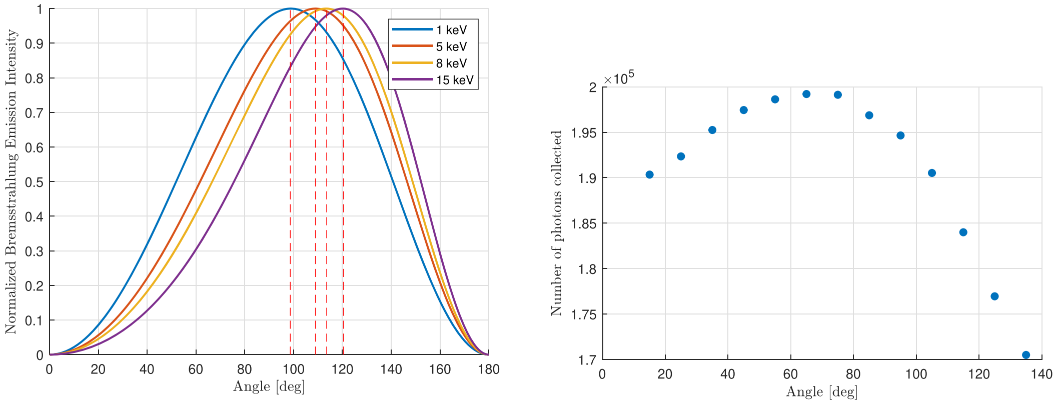

Figure 6. Left: Theoretical bremsstrahlung radiation emission intensity as a function of angle from the incident electron. Right: Variation in number of photons experimentally detected with angle, 8 keV beam and 0 V plate.

between 0 and −2,000 V, while covering an angular range from −30° to +85° relative to target plate normal. The beam energy was kept constant at 8 keV for all tests, while the Inconel target plate was regulated by the power supply.

Peaks were identified for every major component of the target plate. A material composition certificate was available for the Inconel target, which was used to show that peaks could be identified from elements comprising less than 0.5% of the plate mass. Figure 5 shows the estimated plate potential as a function of plate potential at the angle with the largest detected signal. The landing energies at this angle are subtracted from the initial zero plate potential case (the beam energy) to find the relative plate potential. These relative plate potentials are plotted on the left side of Figure 5, while the right plot shows the errors in estimated plate potential.

Bremsstrahlung emission is directionally biased, and the first approximation of bremsstrahlung emission as a function of angle from the incident electron θ and the electron's relativistic velocity $\beta = \frac{v}{c}$ is provided by Van Grieken and Markowicz (2002) as

$$Q(\theta) = \frac{\sin(\theta)^2}{(1 - \beta\cos(\theta))^5}. \tag{2}$$

The magnitude of bremsstrahlung emission Q is therefore a function of angle and landing energy. This relation is plotted in Figure 6, where angles are again relative to the direction of the incident electron beam. The direction of maximum emission is independent of surface or material properties but increases with increasing energy, from 98° for a 1 keV electron to 126° for a 15 keV electron. In addition to changing the directional distribution of bremsstrahlung radiation, electron landing energy also influences the quantity of radiation produced. Efficiency of bremsstrahlung radiation production increases linearly with energy per a description proposed by Kulenkampff and reproduced by Van Grieken and Markowicz (2002), from 5×10^{-5} at 1 keV to 4×10^{-4} at 10 keV, for a nickel target.

The angle between the detector and the target was found to have a significant impact on the accuracy of the landing energy determination, as shown in Figure 7. Figure 7 shows the relationship between angle and accuracy for the 0 V plate case. The error bars indicate the standard deviation for the landing energy data at each angle, where the 0° angle corresponds to the location of the electron beam. The standard deviations increase with increasing angle, indicating less repeatability in measurements, while the errors similarly increase near linearly with angle.

The quantity derived from the bremsstrahlung spectrum is the landing energy of the electrons. This landing energy must be subtracted from a known quantity—the landing energy estimated at either a known plate potential or a known beam energy—in order to determine the plate potential. In this case, the plate potential has its own associated uncertainty, ±30 V. The black points indicate the plate potential determined by subtracting the landing energy from the gun energy, while the magenta points indicate the mean measured value at each plate potential. The dashed blue lines indicate the uncertainty in the power supply regulating the plate potential.

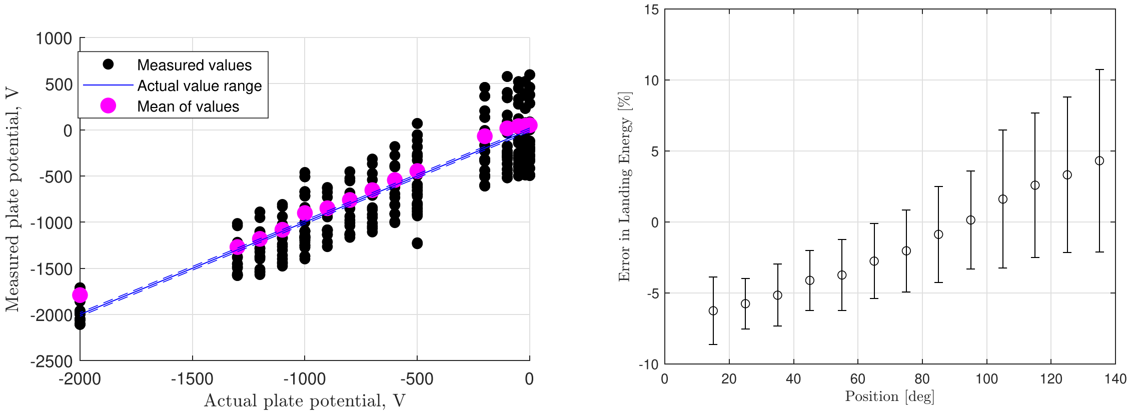

Figure 7. Left: Actual versus measured plate potential from 395 spectra taken at a range of angles, all with 8 keV beam energy. Right: Variation in estimated landing energy as a function of angle, 8 keV beam energy, and 0 V on target plate.

Plate potential magnitudes are clearly underestimated for the −2,000 V plate case in Figure 7. The mean in this case is nearly 200 V off from the actual range, while in the other cases means were far more accurate, with an average error of just 11 V. The beam energies and plate potentials were selected to avoid known limitations of the equipment, maintaining X-ray energies in the range where the detector is most efficient and the power supplies are most reliable. However, no independent system was used to monitor the plate potential at −2,000 V, so it is possible that the power supplies were less reliable here than expected. Additionally, the high plate potential may have been sufficient to perturb the electron beam trajectory, resulting in a different landing angle than expected or electrons landing in a different position on the plate than the detector targeted.

The mean error of the 395 spectra shown in Figure 7 (left) was 14.5 V, which is within the range of uncertainty for the power supply. Attempts to fit Gaussian, Poission, log normal, or extreme value distributions to the observed landing energies were unsuccessful, with each failing to meet commonly accepted statistical significance thresholds. Therefore, to extract an estimate of the uncertainty inherent in the measurements, a bootstrap sampling routine is implemented. Bootstrapping can compute a given statistic by randomly sampling (with replacement) a subset of the full data set and then combining the results of many samplings (DiCiccio & Efron, 1996). In this manner, the mean error for the 395 spectrum set shown in Figure 7 was found to have an uncertainty of ±21 V (with 95% confidence), while the 95% confidence value for any given measurement was found to be 602 V ± 22 V. These values include runs from all angles, which, as seen in the right side of Figure 7, has a significant impact on the accuracy and spread of the measurements. As discussed earlier, the direction of bremsstrahlung radiation is dependent on landing energy, so this plot includes only runs with 8 keV landing energies. A notable takeaway from this plot is that accuracy of the landing energy estimate—and the uncertainty inherent in that estimate—is dependent on the angle between the detector and the incident electron beam.

The variation in landing energy as a function of angle is indicative of the bremsstrahlung spectrum varying with respect to angle. The bremsstrahlung spectrum is known to be doubly differential, in angle and energy, and this is likely the source of this trend. Higher fidelity models for bremsstrahlung emission will help identify the source of this trend and provide a more accurate point of comparison to the experimental photon counts as a function of angle in Figure 6. If this trend is known a priori for a given landing energy, it would be feasible to adjust a computed landing energy from a given angle to improve the accuracy of the result. In addition, the standard deviations of measurements at each location—shown by the error bars in Figure 7 (right)—increase in magnitude with increasing angle. This suggests a greater degree of variability in the sensed spectrum as angle increases, and this is a topic for further investigation.

The landing energy uncertainty for any given run could be reduced through a range of numerical and signal processing techniques (perhaps pursing a support vector machine-based regression model or other transforms) to improve the accuracy of landing energy determination and reduce the sensitivity to noise. Longer collection periods could likewise improve the signal to noise ratio, which might improve the accuracy of the landing energy estimate. Finally, applying filtering techniques, such as the Kalman filter, to a series of estimates made over time or fusing this technique with other methods of remote potential estimation (such as the secondary electron-based method proposed by Bengston & Schaub, 2019) could result in a more accurate potential estimate.

The mean of the errors in landing energy from all angles is -1.1%, but the most accurate measure comes at 95°. Interestingly the direction of peak bremsstrahlung emission, per the first-order model presented by Van Grieken and Markowicz (2002), is approximately 110°. The landing energy accuracy correlates fairly well with the plot shown in Figure 6, which shows the number of photons sensed at each angle for a case with an 8 keV beam and a 0 V plate. In general the measured signal seems to drop off far less, and less quickly, than the predicted signal, though the general shape appears to agree. The bremsstrahlung model used to predict angular distribution of radiation for this case is a basic approximation and does not account for backscatter-induced X-ray generation or other complicating factors which may be responsible for driving the deviations between predicted and observed shapes. Additionally, the experimental values include photon counts from characteristic radiation, which is not included in the bremsstrahlung model. Characteristic radiation is emitted isotropically, which has the effect of adding a baseline flux level to all angles. Radiation emitted from backscattered electrons would be expected dominantly in the angles near the incident electron beam, driving additional deviations between the first-order model and the experimental results shown.

5. Conclusions and Further Work

Prior work has demonstrated the theoretical viability of measuring the potential of a body in space touchlessly, by examining the X-ray spectrum that is generated from an impacting electron beam. Here, the viability of this method has been validated experimentally. Using an electron gun as a source for energetic electrons, it is possible to determine landing energies in a wide range of angles and plate potentials. In addition, this technique allows material composition to be determined simultaneously.

There are several important distinctions between the experimental work here and an actual flight scenario. In this work, all targets were flat plates of a single material charged to a homogenous potential; in a servicing scenario, the target object would be composed of many inhomogenous components, which could also be charged to different potentials. This also introduces higher levels of geometrical complexity, where not only can X-rays be born on multiple surfaces at once from a mixture of ambient hot electrons and the incident electron beam, and those surfaces can have different potentials. In addition, the complex target geometry will result in more complicated electric fields in the vicinity of the target and servicing craft, which will perturb the electron beam used to control the charge on each craft. The electron beam dynamics in the vicinity of large complex charged structures is an area for future work. Additional work by Wilson and Schaub (2020) suggests an approach to use the X-rays generated by hot electrons in the ambient plasma to determine the electrostatic potential of a target body, which could be expanded to examine the limitations of this method for different space weather conditions.

Acknowledgments
The authors would like to thank Dalton Turpen for his assistance in developing experimental equipment and the reviewers for valuable feedback. Data are available as "Dataset for Remote Spacecraft Charge Sensing Experiments" (10.4121/uuid:4b95c725-c78b-430f-8319-188896b1e7b3).

References

Anderson, P. C. (2012). Characteristics of spacecraft charging in low earth orbit. *Journal of Geophysical Research*, *117*, A07308. https://doi.org/10.1029/2011JA016875

Belhaj, M., Jbara, O., Filippov, M. N., Rau, E. I., & Andrianov, M. V. (2001). Analysis of two methods of measurement of surface potential of insulators in SEM: Electron spectroscopy and X-ray spectroscopy methods. *Applied Surface Science*, *177*(1), 58–65. https://doi.org/10.1016/S0169-4332(01)00209-4

Bengtson, M., Hughes, J., & Schaub, H. (2019). Prospects and challenges for touchless sensing of spacecraft electrostatic potential using electrons. *IEEE Transactions on Plasma Science*, *47*(8), 3673–3681.

Bengtson, M. T., & Schaub, H. (2019). Remote sensing of spacecraft potential at geosynchronous orbit using secondary and photo electrons, *AIAA SciTech Forum* (pp. 311). San Diego, CA.

Bengtson, M., Wilson, K., Hughes, J., & Schaub, H. (2018). Survey of the electrostatic tractor research for reorbiting passive GEO space objects. *Astrodynamics*, *2*(4), 291–305.

Bennett, T. J. (2017). On-orbit 3-dimensional electrostatic detumble for generic spacecraft geometries (Unpublished doctoral dissertation), University of Colorado Boulder.

Brandhorst, H. W. J., & Rodiek, J. A. (2007). Improving space utilization by increasing solar array reliability. In *AIAA SPACE 2007 Conference & Exposition, 18–20 September 2007*. Long Beach CA.

Carruth, M. R., Suggs, R., McCollum, M., & Ferguson, D. (2001). Iss and space environment interactions without operating plasma contactor (Tech. Rep.). NASA.

Cazaux, J. (2008). Surface potential and SE detection in the SEM. In M. Luysberg, K. Tillmann, & T. Weirich (Eds.), *EMC 2008 14th European Microscopy Congress 1–5 September 2008, Aachen, Germany* (pp. 519–520). Berlin, Heidelberg: Springer Berlin Heidelberg.

Deslattes, R. D., Kessler, E. G., Indelicato, P., de Billy, L., Lindroth, E., & Anton, J. (2005). X-ray transition energies database. https://doi.org/10.18434/T4859Z

DiCiccio, T. J., & Efron, B. (1996). Bootstrap confidence intervals. *Statistical Science*, *11*(3), 189–228. https://doi.org/10.1214/ss/1032280214

Duane, W., & Hunt, F. (1915). On X-ray wave-lengths. *Physical Review*, *6*, 166–172. https://doi.org/10.1103/PhysRev.6.166

Engwerda, H. (2017). Remote sensing for spatial electrostatic characterization using the multi-sphere method (Unpublished master's thesis), Delft, The Netherlands.

Ferguson, D. C., Hoffmann, R. C., Engelhart, D. P., & Plis, E. A. (2017). Voltage threshold and power degradation rate for GPS solar array arcing. *IEEE Transactions on Plasma Science*, *45*(8), 1972–1975. https://doi.org/10.1109/TPS.2017.2694387

Ferguson, D. C., Murray-Krezan, J., Barton, D. A., Dennison, J. R., & Gregory, S. A. (2014). Feasibility of detecting spacecraft charging and arcing by remote sensing. *Journal of Spacecraft and Rockets*, *51*(6), 1907–1913.

Goodman, M., Paez, A., Willis, E., & DeStefano, A. (2019). An analytic model for estimating the first contact resistance needed to avoid damaging ESD during spacecraft docking in GEO. In *Applied Space Environments Conference*. Los Angeles, CA.

Halekas, J., Delory, G., Brain, D., Lin, R., FIllingim, M., Lee, C., et al. (2007). Extreme lunar surface charging during solar energetic particle events. *Geophysical Research Letters*, *34*, L02111. https://doi.org/10.1029/2006GL028517

Heath, J. T., Jiang, C.-S., & Al-Jassim, M. M. (2012). Measurement of semiconductor surface potential using the scanning electron microscope. *Journal of Applied Physics*, *111*(4), 046103. https://doi.org/10.1063/1.3684556

Hogan, E. A. (2014). Impacts of tug and debris sizes on electrostatic tractor charging performance. *Advances in Space Research*, *55*(2), 630–638.

Karavaev, Y. S., Kopyatkevich, R. M, Mishina, M. N., Mishin, G. S., Papushev, P. G., & Shaburov, P. N. (2004). The dynamic properties of rotation and optical characteristics of space debris at geostationary orbit. *Advances in the Astronautical Sciences*, *4*(119), 1457–1466.

Katz, I., Davis, V. A., & Snyder, D. B. (1998). Mechanism for spacecraft charging initiated destruction of solar arrays in GEO.

King, L. B., Parker, G. G., Deshmukh, S., & Chong, J.-H. (2002). Spacecraft formation-flying using inter-vehicle coulomb forces (Tech. Rep.): NASA/NIAC.

King, L. B., Parker, G. G., Deshmukh, S., & Chong, J.-H. (2003). Study of interspacecraft Coulomb forces and implications for formation flying. *AIAA Journal of Propulsion and Power*, *19*(3), 497–505.

Lai, S. T. (2011). *Fundamentals of spacecraft charging: Spacecraft interactions with space plasmas*. Princeton, NJ: Princeton University Press.

Lamoureux, M., & Charles, P. (2006). General deconvolution of thin-target and thick-target bremsstrahlung spectra to determine electron energy distributions. *Radiation Physics and Chemistry*, *75*(10), 1220–1231.

Moore, C. S., Caspi, A., Woods, T. N., Chamberlin, P. C., Dennis, B. R., Jones, A. R., et al. (2018). The instruments and capabilities of the miniature X-ray solar spectrometer (MinXSS) cubeSats. *Solar Physics*, *293*(2). https://doi.org/10.1007/s11207-018-1243-3

Mullen, E. G., Gussenhoven, M. S., Hardy, D. A, Aggson, T. A., & Ledley, B. G. (1986). Scatha survey of high-voltage spacecraft charging in sunlight. *Journal of Geophysical Research*, *91*(A2), 1474–1490.

Reed, B. B., Smith, R. C., Naasz, B. J., Pellegrino, J. F., & Bacon, C. E. (2016). The restore-l servicing mission, *AIAA space 2016*. https://doi.org/10.2514/6.2016-5478

Schaub, H., & Moorer, D. F. (2014). Geosynchronous large debris reorbiter: Challenges and prospects. *The Journal of the Astronautical Sciences*, *59*(1-2), 161–176.

Schindelin, J., Arganda-Carreras, I., & Frise, E. (2012). Fiji: An open-source platform for biological-image analysis. *Nature Methods*, *9*, 676–682.

Van Grieken, R. E., & Markowicz, A. A. (Eds.) (2002). *Handbook of X-ray spectrometry* (2nd ed.). Marcel Dekker, Inc.

Wilson, K., & Schaub, H. (2019). X-ray spectroscopy for electrostatic potential and material determination of space objects. *IEEE Transactions on Plasma Science*, *47*(8), 3673–3681.

Wilson, K., & Schaub, H. (2020). An X-ray spectroscopic approach to remote space object potential determination: Experimental results, *AIAA SciTech Forum*. Orlando, FL. https://doi.org/10.2514/6.2020-0049

Xr-100cr Si-PIN X-ray detector (2018) (Tech Rep). Amptek, Inc.